

Misidentification of Short GRBs as Magnetars in Nearby Galaxies

Elisa C. Schösser^{1,2,3*}, J. Michael Burgess¹, and Jochen Greiner¹

¹ Max-Planck-Institut für Extraterrestrische Physik, Giessenbachstrasse 1, 85748 Garching, Germany, e-mail: jburgess@mpe.mpg.de

² Technische Universität München, Physik-Department, James-Frank-Str. 1, 85748 Garching bei München, Germany

³ Zentrum für Astronomie der Universität Heidelberg, Astronomisches Rechen-Institut, Mönchhofstr. 12-14, 69120 Heidelberg, Germany, e-mail: elisa.schoesser@uni-heidelberg.de

ABSTRACT

Context. Recent observations of GRB 200415A, a short and very bright pulse of γ -rays, have been claimed to be an extragalactic magnetar giant flare (MGF) whose proposed host galaxy is the nearby NGC 253. However, as the redshift of the transient object was not measured, it is possible that the measured location of the transient on the celestial sphere and the location of the local galaxy merely coincided. Thus, its real progenitor could have been arbitrarily far away, leading possibly to a much larger luminosity of the transient, and leaving the standard model of short gamma-ray bursts (sGRBs), the merger of two compact objects, as an explanation for the observations.

Aims. In this study, our aim is to compute the false-alarm rate for the misinterpretation of sGRBs as magnetars in a given observation period.

Methods. We simulate synthetic surveys of sGRB observations in a time period of 14 years corresponding to the operation period of the Gamma-ray Burst Monitor (GBM) detector. For all sGRBs that align on the sky with a nearby Local Volume galaxy, we generate realistic data which is folded through the response of the GBM. To identify candidates of sGRBs that may be misinterpreted as magnetars, six selections (spatial, star formation rate, GBM trigger, duration, isotropic energy release, and fluence) are applied to the simulated surveys.

Results. In a non-negligible fraction, 15.7 %, of the simulated surveys, we identify at least one sGRB that has the same characteristics as a magnetar giant flare and could be thus misinterpreted as magnetar. Thus, we conclude that the selections that were proposed in previous work to unambiguously identify an extragalactic magnetar giant flare are not sufficient.

Key words. methods:statistical – methods:data analysis – gamma-ray burst: general

1. Introduction

Time-domain astronomy is a rapidly growing field with ever more instruments dedicated to measuring transient events in the sky. As the number of events grow, the likelihood of chance coincidence between these events or with temporally static astrophysical objects also grows. In this young field, the proper statistical techniques to compute these chance coincident detection probabilities do not fully exist. Frustrating the problem further is that often there are not physical models for the source rates, cosmological distribution, and/or source production processes which would allow for one to rule out chance association with purely astrophysical arguments. When the events are rare or even from unexplained origins, the problem intensifies. Herein, we examine one such association where a transient gamma-ray event spatially coincided with a nearby galaxy in attempt to determine the probability that this association was misidentified.

There are two known astrophysical sources that emit short, transient pulses of γ -rays, namely magnetars and short gamma-ray bursts (GRBs). With luminosities of up to 10^{54} erg s⁻¹ (Frederiks et al. 2013), GRBs are the most luminous explosions in the electromagnetic spectrum known in the universe. The prompt emission of GRBs peaks in the γ -ray band, and is followed by an afterglow that may be detectable in the X-ray, optical and ra-

dio wavelengths, if the follow-up observations are fast and sensitive enough. Typically, GRBs are classified by their duration into short (< 2 s) and long GRBs (> 2 s) (Mazets et al. 1981). Short GRBs (sGRBs) are associated with the merger of two compact objects, which was confirmed by the joint detection of a short GRB and a gravitational wave (GW 170817) in 2017 (Abbott et al. 2017).

First indicated by their isotropic spatial distribution on the sky and later confirmed by redshift measurements, it was shown that GRBs originate at cosmological distances (Metzger et al. 1997). From absorption lines in the optical afterglow spectrum, the redshift can be directly determined. However, this is not always possible, as the intensity of the optical afterglow decays rapidly with time, and is often lower than the detection limit at the time of follow-up observations. Thus, the most frequently used method for determining the redshift is to attempt to identify a host galaxy of the GRB and measure its distance. Only about 24 % of all GRBs have determined redshifts¹. The search for host galaxies in the field of view can lead to wrong associations, especially if the GRB's localization error is larger than a few arcseconds. The existence of a bright galaxy in the field of view that potentially has a large angular size may prevent the detection of the dimmer true host of the GRB. One recent example for an initial wrong association of a GRB with a galaxy that was later discarded by deeper follow-up observations was

* Fellow of the International Max Planck Research School for Astronomy and Cosmic Physics at the University of Heidelberg (IMPRS-HD)

¹ Statistic from <https://www.mpe.mpg.de/~jcg/grbgen.html>

the detection of GRB 220611A. First, the GRB triggered the Swift Burst Alert Telescope (Cenko et al. 2022) and the GRB was localized with an uncertainty of 3 arcmin. A nearby galaxy with redshift $z = 0.049$ was proposed as a candidate for the host galaxy as it had an angular distance of 15 arcsec from the GRB. Later, Rastinejad et al. (2022) found another faint optical source in the Legacy Survey (Dey et al. 2019) that coincided with the location of the detected GRB. A follow-up observation with Chandra lead to the detection of the GRB’s X-ray afterglow and decreased the uncertainty of the localization to only 0.5 arcsec (Levan et al. 2022). At exactly that 0.5 arcsec transient location, the host galaxy was identified, and spectroscopically determined to be at $z=2.36$ (Schneider et al. 2022). Prior to this identification the association to the much brighter, nearby galaxy was (wrongly) preferred.

Magnetars, on the other hand, are believed to be young and strongly magnetized neutron stars with a magnetic field strength of $10^{13} - 10^{15}$ G (Duncan & Thompson 1992). Magnetic stresses at the core-crust boundary or instabilities in the magnetic field can cause the sudden ejection of magnetic energy which can be observed as repeating short bursts in the X-rays and soft γ -rays (Thompson & Duncan 1993). Magnetars are mainly found within the Milky Way and were discovered by the detection of recurrent short bursts in the X-rays and soft gamma-rays with luminosities of about 10^{40} erg s^{-1} . Observations of flares with an energy output of more than 10^{44} erg s^{-1} , called magnetar giant flares (MGFs), were observed for three already known magnetars after an increase in activity, SGR 0526-66 (Evans et al. 1980; Mazets et al. 1979), SGR 1900+14 (Hurley et al. 1999; Mazets et al. 1999), and SGR 1806-20 (Palmer et al. 2005; Mereghetti et al. 2005). These three magnetars are of galactic origin, and were characterized by an initial strong pulse followed by a long tail with quasi-periodic oscillations (QPOs) in the frequencies between 18 and 626.5 Hz (Barat et al. 1983; Israel et al. 2005; Strohmayer & Watts 2005; Watts & Strohmayer 2006; Pompe et al. 2018). Recurrent MGFs have not been observed yet.

The total released energy of $(2 - 3) \times 10^{46}$ erg of the SGR 1806-20 giant flare suggested that MGFs may be detectable up to distances of about 50 Mpc, including other nearby galaxies as origin (Hurley et al. 2005). This finding motivated searches in measured data of sGRBs to identify a fraction of GRBs that can be associated with nearby galaxies and can thus be explained by MGFs (Tanvir et al. 2005; Tikhomirova et al. 2010; Svinkin et al. 2015; Mandhai et al. 2018). Following this campaign, additional extragalactic MGF candidates were proposed, namely GRB 051103 (Ofek et al. 2006), GRB 070201 (Mazets et al. 2008; Ofek et al. 2008), GRB 070222 (Burns et al. 2021), and most recently GRB 200415A (Svinkin et al. 2021; Roberts et al. 2021). The main argument for the interpretation of the observations as magnetar giant flares was the coinciding locations of the detected γ -rays with nearby galaxies that have a distance smaller than 5 Mpc. GRB 051103 was found to coincide with the location of the M81/M82 galaxy group, GRB 070201 was associated with the Andromeda Galaxy, GRB 070222 with M83, and GRB 200415A with NGC 253. However, no distance estimate was possible for any of the proposed extragalactic MGFs. Thus, it cannot be excluded that the origin of the gamma-rays is at much farther distances beyond the associated galaxies. As the measured flux scales approximately as $\propto 1/r^2$, a larger distance r would correspond to a higher luminosity of the source. Beyond a certain distance (1-2 Mpc), the origin of gamma-rays from magnetars becomes unlikely, leaving sGRBs as natural explanation. Thus, a distance estimate is crucial for the distinction of magnetar vs. sGRB interpretation.

Table 1. Medians, modes, means, and 90 % credible intervals (C.I.) of the marginal posterior distributions of the T_{90} fit for the means (μ_1, μ_2), standard deviations (σ_1, σ_2) and the mixture parameter (θ).

Parameter	Median	Mode	Mean	90 % C.I.
μ_1	-0.20	-0.20	-0.19	(-0.29,-0.07)
μ_2	1.44	1.43	1.40	(1.40,1.50)
σ_1	0.54	0.55	0.55	(0.46,0.65)
σ_2	0.46	0.46	0.46	(0.44,0.47)
θ	0.22	0.20	0.20	(0.20,0.30)

Given that all claimed extragalactic magnetars observations lack a distance estimate, the aim of this work is to compute the probability for the misinterpretation of an sGRB as a magnetar due to chance alignment with a nearby galaxy. To do so, we generate a population of sGRBs as seen by Fermi-GBM via sampling all population parameters from observationally motivated distributions. We select the sGRBs that are spatially coincident with nearby galaxies. For the chosen sGRBs, we simulate realistic GBM data, analyze the simulated data, and select candidates for misinterpretation as magnetars based on multiple selection criteria that were applied in the past to identify extragalactic MGFs.

The article is structured as follows: In Sec. 2, we describe the generative model used for the population synthesis. In the subsequent Sec. 3, we explain how we simulate Fermi-GBM data. How we analyze the simulated data is summarized in Sec. 4. We summarize the selection criteria in Sec. 5, which we apply to our sGRB surveys to identify candidates for misinterpretation as extragalactic MGFs. To proof the consistency of our simulations, we performed tests which are presented in Sec. 6. Finally, we show our results in Sec. 7, and summarize our conclusions in Sec. 8.

2. SGRB population synthesis

To simulate a population of sGRBs, we sample the latent parameters from distributions which are motivated by observations. The latent parameters of sGRBs include their sky coordinates, luminosity, distance, duration, and the parameters describing their spectral evolution. The right ascension and declination of the simulated GRBs is drawn in such a way that they are uniformly distributed on the sphere. In the following, we describe our chosen distributions for the other parameters.

2.1. Duration, light curve and spectral shape

In all simulations, we model the sGRBs with a constant light curve over the burst duration. We note that this simplifies the realistic pulse profile of real sGRBs but is necessitated by computation costs. The inclusion of realistic profiles does not change our results.

The measured duration (T_{90}) distribution is fitted with a mixture model of two log-normal distributions. We use the measured durations of all 3291 GRBs in the public Fermi/GBM catalog (von Kienlin et al. 2020). For the fit, we use the Bayesian framework Stan (Carpenter et al. 2017). The uncertainty of the posterior fit is depicted in Figure 1. The chosen median best fit distribution function for sGRBs that we use in this work is highlighted in orange.

In Table 1, the median, mode, mean, and 90 % credible intervals (C.I.) of all fit parameters are listed. The best-fit parameters are in similar range as the previous fit results in von Kienlin et al.

(2020). Only the result for the standard deviation differs approximately by a factor of two for both short and long GRBs. The median best fit mixing parameter of 0.22 yields that 22 % of the GRBs in the sample are sGRBs, corresponding to 724 GRBs.

In this study, we draw the duration T_{90} of the sGRBs from a \log_{10} -normal distribution with a probability density function that is given by

$$p(T_{90}) = \frac{1}{\sqrt{2\pi}\sigma_1 T_{90} \ln(10)} \exp\left(-\frac{1}{2}\left(\frac{\log_{10}(T_{90}) - \mu_1}{\sigma_1}\right)^2\right), \quad (1)$$

where we use for the mean μ_1 and standard deviation σ_1 , the median best-fit parameters as summarized in Table 1.

It was shown that the largest fraction (69 %) of GRB prompt emission spectra are best fit by a cutoff power law (CPL) when compared to three other empirical models, including the Band function (9.3 %), a smoothly broken power law (11.4 %), and a simple power law (10.2 %) (Yu et al. 2016). Thus, we model the spectra of the sGRBs with CPLs. The CPL function is parameterized as

$$N(E; K, E_p, \alpha) = K \left(\frac{E}{E_{\text{piv}}}\right)^\alpha \exp\left(-\frac{(2 + \alpha)E}{E_p}\right). \quad (2)$$

Here, K is the normalization flux given in $\text{cm}^{-2} \text{s}^{-1} \text{keV}$ at the pivot energy E_{piv} , and α is the spectral index at low energies. In the νF_ν representation, the spectrum has its peak at E_p which is given in keV.

The distribution for E_p is chosen to be the same as the best-fit distribution in Ghirlanda et al. (2016) which is a broken power law function. The parameters of the distribution are summarized in Table 2. Instead of fixing the power law index α as in Ghirlanda et al. (2016), α is drawn from a truncated normal distribution with a mean of $\mu_\alpha = -0.6$ and a standard deviation $\sigma_\alpha = 0.2$ in the interval $[-1.5, 0]$. The chosen distribution for α is motivated by the results from Burgess et al. (2019).

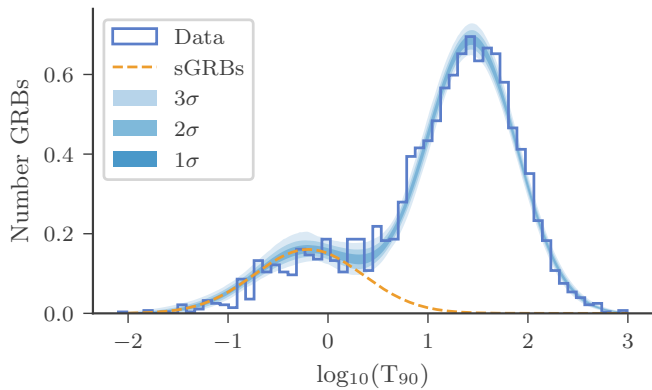


Fig. 1. Histogram of the measured $\log_{10}(T_{90})$ data from GBM. Blue shaded: 68.3 % (1 σ), 95.5 % (2 σ), and 99.7 % (3 σ) quantiles of the posterior T_{90} distribution of the mixture model. Orange dashed line: Best fit normal distribution for the durations of sGRBs using the medians of the parameters' marginal posterior distributions.

2.2. Redshift and Luminosity Distribution

To determine the redshift and luminosity distribution from observations is a non-trivial task as the observed flux is both dependent on the luminosity and redshift. Furthermore, as a result of various selection effects, the sample of detected GRBs is not

representative of the underlying population. One of the selection effects is the so-called Malmquist bias which describes the effect of preferably detecting bright sources. In comparison to long GRBs, it is even more challenging to determine the redshift and luminosity distribution for short GRBs as there is only a very small number of sGRBs with measured redshift, thus enhancing the selection effects for sGRBs immensely. Nevertheless, there were multiple attempts in the past to determine the redshift and luminosity function of sGRBs by fitting the measured peak flux distribution and redshifts (e.g. Guetta & Piran 2005, 2006; Nakar et al. 2006; Virgili et al. 2011; D'Avanzo et al. 2014; Wanderman & Piran 2015). With the aim of decreasing selection effects and obtaining a representative sample of GRBs, often a flux limit is set when choosing the GRBs. In addition to using the peak flux distribution, Ghirlanda et al. (2016) include measurements of the peak energy of the observed spectra, the fluence, the duration, and if the redshift is known, the isotropic equivalent luminosity and energy, for the fits.

In this work, we sample the luminosity L and redshift z from the fitted distributions $\Phi(L)$ and $\rho(z)$ in Ghirlanda et al. (2016). Assuming that the bursting rate of GRBs is proportional to the star formation rate, the following parameterization of the redshift distribution

$$\rho(z) = \rho_0 \Delta t_{\text{obs}} \frac{1 + p_1 z}{1 + (z/z_p)^{p_2}}, \quad (3)$$

is used, as in Cole et al. (2001). The parameter ρ_0 is the rate of GRBs at redshift zero and has the units of $\text{yr}^{-1} \text{Gpc}^{-3}$, and Δt_{obs} is the observation period of the survey. The rise, location of the peak, and decay of the redshift distribution are all influenced by the parameters z_p , p_1 , and p_2 . The chosen redshift distribution is independent of the emission properties of the GRBs, which implies the underlying assumption that the emission properties do not change with cosmic time.

For the peak energy E_p , a broken power law distribution was chosen which has the probability density function

$$p(E_p) \propto \begin{cases} (E_p/E_{p,\text{break}})^{-a} & E_p \leq E_{p,\text{break}} \\ (E_p/E_{p,\text{break}})^{-b} & E_p > E_{p,\text{break}} \end{cases} \quad (4)$$

where $E_{p,\text{break}}$ is the break energy at which the power law index changes from $-a$ to $-b$.

We use the results of case (c) in Ghirlanda et al. (2016), in which no correlation between the peak energy E_p and the isotropic equivalent energy L_{iso} is assumed. Thus, we draw the luminosity from the fitted independent distribution, a broken power law distribution function

$$\Phi(L) \propto \begin{cases} (L/L_b)^{-\alpha_1} & L \leq L_b, \\ (L/L_b)^{-\alpha_2} & L > L_b. \end{cases} \quad (5)$$

The modes of the best-fit parameters from Ghirlanda et al. (2016) for the redshift, peak energy, and luminosity distribution that we use in this work are summarized in Table 2.

2.3. Number of objects in Simulated sGRB Surveys

The total number of GRBs N within the volume with maximum distance z_{max} that is expected to be observed during the observa-

Table 2. Modes of all fitted parameters in case (c) from the Monte Carlo Markov Chain results from Ghirlanda et al. (2016).

Parameter	$\dot{\rho}_0$ [$\text{yr}^{-1} \text{Gpc}^{-3}$]	p_1	p_2	z_p	a	b	E_{pb} [keV]	α_1	α_2	L_b [$10^{52} \text{erg s}^{-1}$]
Mode (c)	0.8	2.0	2.0	2.8	-0.55	2.5	2100	-0.32	1.8	0.79

tion period of Δt_{obs} is computed by

$$N = \int_0^{z_{\text{max}}} \frac{c d_L^2 \dot{\rho}'(z)}{(1+z)^3 H_0 \sqrt{\Omega_m(1+z)^3 + \Omega_\Lambda}} dz \int d\Omega \int_{\Delta t_{\text{obs}}} dt, \quad (6)$$

$$= \Delta t_{\text{obs}} D \int_0^{z_{\text{max}}} \frac{c d_L^2 \dot{\rho}'(z)}{(1+z)^3 H_0 \sqrt{\Omega_m(1+z)^3 + \Omega_\Lambda}} dz, \quad (7)$$

where D is the duty cycle of the telescope. The duty cycle of GBM is approximately 60 % (Fermi-LAT and GBM Collaboration 2022) which describes the times per day at which the instrument is shut down when flying through the South Atlantic Anomaly (SAA), and due to the fraction of the sky which is occulted by Earth. For all simulations of a survey of sGRBs, a total observing period of $\Delta t_{\text{obs}} = 14$ years was chosen, corresponding approximately to the time since GBM was launched in 2008.

2.4. Summary of Simulated Parameters and their Distributions

In this work, we use the object-oriented astrophysics population synthesis framework `popsynth`² (Burgess & Capel 2021). Once the population is set up and all parameter distributions and dependencies are chosen, the expected total number of objects is computed by integrating the spatial rate distribution. The number of detected GRBs in the survey is then drawn from a Poisson distribution and for all objects in the survey, the latent and observed quantities defining the population are drawn, including the distances and luminosities of the objects. The final population object containing all sampled parameters is saved as an HDF5 file for later analysis. In Fig. 2, all sampled parameters, and their distributions (with needed parameters) are summarized.

3. Simulating GBM Data

Once the population of objects is created, we simulate Fermi-GBM data so that we can analyze its properties and have realistic event triggers. In order to obtain realistic GBM data for GRBs in the simulated sample, we designed a generic software package `cosmogrb`³ which accepts as input a population of latent parameters generated with `popsynth` and outputs a corresponding catalog of synthetic GBM Time-tagged event (TTE) data for all detectors for each GRB. These data can then be analyzed as if they were an authentic GRB observation both to determine if the event would have resulted in a GBM trigger alert as well as for routine spectral analysis. The steps of the simulation are detailed below.

3.1. Orbit and Detector Response

As the orientation of the various GBM detectors with respect to a transient event is crucial to both the detection and observed

spectral data properties of the event, we must simulate how the detectors' orientation changes with respect to the celestial sky as GBM orbits the Earth. To achieve this, `cosmogrb` takes as input the so-called position history file which details both the orbital location of the Fermi spacecraft as well as its zenith pointing. Thus, we fully account for the rocking motion performed by Fermi so that the Large Area Telescope (LAT) can observe the full sky. For a given simulated GRB event, a random point within the orbit is selected. With the orientation of the GBM detectors set for the observation, this orientation and the celestial location of the simulated GRB are passed to `gbmdrmgen`⁴ which is used to generate the correct detector responses for all GBM detectors corresponding to the event.

3.2. Spectrum Simulation

With the detector responses defined for the observation, the latent source spectrum can be folded through these responses to create the observed counts as the spectrum evolves with time. In order to create these counts, the spectrum as a function of time and energy is multiplied by a GBM detector's effective area as a function of energy and then integrated over energy to compute the total photon flux as a function of time. This is then used to sample the exponentially distributed arrival times of the observed counts. This sampling is done via a rejection scheme for an inhomogeneous Poisson process as described in Burgess et al. (2021). Once the arrival times have been selected, they are passed to the effective area weighted source spectrum as the given time which is then rejection sampled over energy to obtain the energy of the observed photon. This energy is then redshifted and passed to the energy redistribution function corresponding to its value to compute the sampled PHA channel of the count. The end result are time-tagged counts corresponding to PHA channels which can then be converted to the standard GBM TTE data format for each detector.

In order to add a background to each observation in each detector, `cosmogrb` uses a set of template background count spectra which have their amplitudes randomized to reflect the observed variations in the GBM background. The backgrounds are assumed to be constant in time and have their count arrival times sampled as described above. The PHA channels of the simulated counts are then sampled after being weighted with the distributions from the templates.

4. Analysis of GBM Data

We analyze the simulated data using the same framework as previously detected GRBs in the past using the Multi-Mission Maximum Likelihood (3ML) framework (Vianello et al. 2015)⁵. Our spectral analysis is based on the same methodology as presented in Burgess et al. (2019).

For all simulated GRBs that were selected by the GBM trigger, we analyze the simulated data. We use the Bayesian block algorithm (Scargle et al. 2013) to find significant changes in the

² <https://github.com/grburgess/popsynth>

³ <https://github.com/grburgess/cosmogrb>

⁴ https://github.com/grburgess/gbm_drm_gen

⁵ <https://github.com/threeML/threeML>

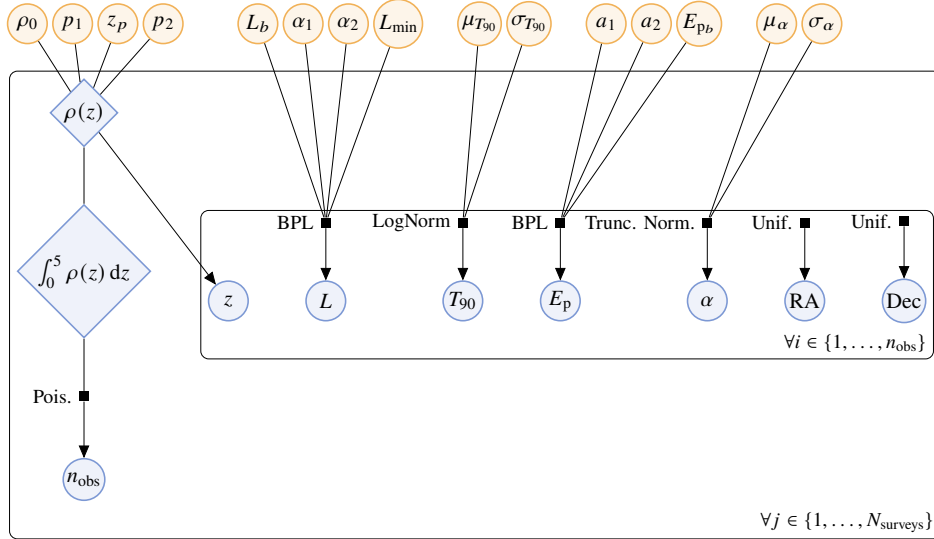


Fig. 2. Probabilistic graphical model summarizing all sampled latent parameters (**blue circles**) of each GRB with a constant temporal profile using the parameters defined in case (c) of Ghirlanda et al. (2016) for the luminosity L , redshift z , and peak energy E_p distribution. The hyperparameters defining the used probability density distributions are highlighted with **orange circles**.

count rates. If less than three time bins are found by the algorithm, and thus no significant flux increase is found, we stop the GRB analysis, and we discard the GRB from the sample.

If three or more time intervals are found, we fit the background in the first and last time interval with a constant by maximizing the Poisson likelihood that is given by

$$\mathcal{L} = \prod_{i=1}^N \frac{M^{B_i} e^{-M}}{B_i!}, \quad (8)$$

where N is the number of time bins, M is the number of model counts given by the constant background rate, and B_i is the number of measured background counts (Greiner et al. 2016).

We use profile likelihoods in which the likelihood is only evaluated at the values for α_b that minimize the negative log-likelihood function for specific constant source parameters α_s

$$-\ln \mathcal{L}(\alpha_s) = \min_{\alpha_b} [-\ln(\mathcal{L}(\alpha_s, \alpha_b))], \quad (9)$$

as described in Vianello et al. (2015). After the background model \tilde{B} is fitted in the off-source time period, it has Gaussian uncertainties with standard deviation $\sigma_{\tilde{B}}$. In contrast, the total counts are still Poisson distributed. Thus, a Poisson-Gaussian likelihood is needed to fit the spectral model to the data. To do so, we use the so-called PG-statistic⁶

$$-2 \ln \mathcal{L} = 2 \sum_{i=1}^N M_i + t_s f_i - S_i \ln(M_i t_s f_i) + \frac{(\tilde{B}_i - t_s f_i)^2}{2\sigma_{\tilde{B},i}^2} - S_i (1 - \ln S_i) \quad (10)$$

for each i^{th} energy bin. Here, N is the number of total counts, S_i is the number of measured source counts, M_i is the predicted number of counts based on the model and the response, t_s is the source time interval, and f_i is the profiled-out background model which is derived by setting the derivative of the likelihood as

⁶ Definition is taken from <https://heasarc.gsfc.nasa.gov/xanadu/xspec/manual/XSappendixStatistics.html>.

in Equation (9) to zero. The spectrum is rebinned in such a way that there is at least one count per bin, as this is required for using profile likelihoods. We use nested sampling (MultiNest (Feroz et al. 2009; Buchner et al. 2014)) for computing the posterior distributions.

Once, the time-integrated spectrum $N(E; K, E_p, \alpha)$ is fitted, we can compute the total isotropic energy release over the standard $1 - 10^4$ keV range for a given source time interval Δt by integrating the observed time-integrated spectrum over energy

$$E_{\text{iso}, \Delta t} = 4\pi d_L^2 \int_{1 \text{ keV}}^{10^4 \text{ keV}} E N(E; K, E_p, \alpha) dE. \quad (11)$$

By summing the computed isotropic energy from all found source time intervals, the total isotropic energy release can be determined.

5. Selection Criteria

For the search of MGF candidates in the simulated universes of GRBs, we implemented multiple selections that are motivated by the selection criteria that were used to identify extragalactic MGFs in the past. The selection criteria are summarized in the following.

5.1. Spatial Selection

The first selection is applied to the sampled GRB coordinates. We only select GRBs that can be associated on the sky with a nearby galaxy. We use the Local Volume (LV) Galaxy catalog of Kaisina et al. (2012)⁷ which currently contains information about 1246 galaxies up to a distance of 11 Mpc from the Milky Way. The catalog is an extension of the Catalog of Neighboring Galaxies (Karachentsev et al. 2004).

For all LV galaxies, the center of the galaxy on the sky is given by its right ascension ϕ_{cen} , and declination θ_{cen} . We approximate the form of a galaxy as an ellipse which is projected

⁷ <https://www.sao.ru/lv/lv gdb>

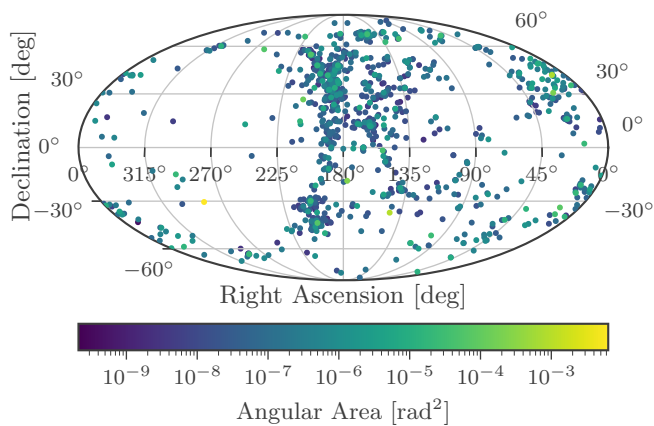


Fig. 3. Location of the Local Volume galaxies on the sky in ICRS coordinates as given in the catalog of Kaisina et al. (2012). The color illustrates the angular extent of the galaxies.

onto a sphere with distance d , with semi-major and semi-minor angular axis, α and β respectively. The angular size of the elliptical galaxies is then given by $A = \pi \alpha \beta$. In the sky map in Fig. 3, the location of all galaxies and their angular size are shown. For the coordinates, we use the International Celestial Reference Frame (ICRS). As the Large and Small Magellanic Cloud would dominate the results with their exceptional large angular sizes of $A_{LMC} = 8.6 \times 10^{-2} \text{ rad}^2$ and $A_{SMC} = 2.2 \times 10^{-2} \text{ rad}^2$, we excluded them from our analysis.

When a GRB triggers a detector, its angular coordinates ϕ_{GRB} , θ_{GRB} are determined within uncertainties. Without knowing the distance to the GRB, the host galaxy of the GRB can never be securely determined. From the perspective of an observer on Earth, the GRB coincides with the location of a galaxy if the projected GRB's uncertainty region overlaps with the elliptic galaxy (see Fig. 4).

Using spherical coordinates, the ellipse equation of a galaxy that is centered at the origin, is symmetric around the \mathbf{e}_r axis, and has its major and minor axis aligned with the \mathbf{e}_ϕ and \mathbf{e}_θ axis, is given by

$$\left(\frac{\phi}{\alpha}\right)^2 + \left(\frac{\theta}{\beta}\right)^2 \leq 1. \quad (12)$$

To find out whether the GRB's uncertainty circle and galaxy's ellipse intersect, we first evaluate the relative two-dimensional vector

$$\mathbf{r} = \mathbf{r}_{\text{GRB}} - \mathbf{r}_{\text{cen}} \quad (13)$$

between the galactic center \mathbf{r}_{cen} and the GRB's position \mathbf{r}_{GRB} . The orientation of the galaxies on the sky is given by their rotation angle γ that is defined in the \mathbf{e}_ϕ , \mathbf{e}_θ plane (see Fig. 4). As the rotation angle is not given in the catalog, we sample it for each galaxy from a uniform distribution between 0° and 180° with a fixed seed and thus keep the orientation constant in all simulated universes. As it is easier to rotate a vector instead of changing the ellipse equation, the vector \mathbf{r} is rotated in the opposite direction by the angle γ , yielding the vector $\mathbf{r}_{\text{GRB,new}}$. If the GRB's rotated relative vector $\mathbf{r}_{\text{GRB,new}}$ fulfills Equation (12) for a galaxy, we assume an association between the GRB and the galaxy and select the GRB for further studies.

Assuming the GRB's location is measured within a circle of radius δ_{err} , the GRB is associated with an elliptic galaxy if the

error circle of a GRB and the elliptical galaxy intersect. So, in addition to the center of the GRB's location, we test if at least one of three more points, P_1 , P_2 or P_3 , lie within the galaxy's ellipse (see Fig. 4). We define the point P_1 as the intersection point between the line connecting the galaxy's center with the GRB's center (see Fig. 4). The points P_2 and P_3 are defined by the intersection of the line between the focus points, F_1 and F_2 , and the center of the rotated GRB, given by $\mathbf{r}_{\text{GRB,new}}$, with the GRB's outer radius. The distance of the two focus points to the center of the ellipse is given by $\epsilon = \sqrt{\alpha^2 - \beta^2}$.

Note here, that there are cases in which all three points lie outside the ellipse but the ellipse and the circle intersect nonetheless (see right panel in Fig. 4). As this is only the case when the intersection area between the ellipse and circle is small, we neglect these edge effects because an association is very unlikely to be made when the intersection is so weak.

5.2. GBM Trigger Selection

To find out which of the sGRBs in the simulated universe would be detected by GBM, the trigger algorithm of GBM is applied to the simulated GRB data.

A detailed overview of GBM's trigger algorithm is given in Meegan et al. (2009) and Paciesas et al. (2012). GBM's detectors are triggered when in at least two detectors an increase of the measured background subtracted rate is measured that is above a specified threshold. The significance s is defined as

$$s = \frac{N_s - \Delta t_s \frac{N_b}{\Delta t_b}}{\sqrt{\Delta t_s \frac{N_b}{\Delta t_b}}}. \quad (14)$$

Here, N_s is the number of counts measured in the source time interval Δt_s , and N_b is the number of background photons that were detected in the previous time interval Δt_b . The background rate $N_b/\Delta t_b$ is defined as the average rate that is obtained from the 17 s before the start of the tested source time interval. As threshold, $s > 4.5$ is set as default in `cosmogrb`. Note here, that the chosen significance definition was shown to yield incorrect results (Li & Ma 1983). Nonetheless, we use it to imitate GBM's onboard trigger algorithm.

The significance is computed for four different energy ranges, (1) 50 – 300 keV, (2) 25 – 50 keV, (3) > 100 keV, and (4) > 300 keV. For the energy ranges (1) and (2), ten time scales for Δt_s between 16 ms and 8.192 s were tested, successively increasing as $16 \text{ ms} \cdot 2^n$ with $n \in [0, 1, \dots, 9]$. The tested time scales for (3) include only the first nine time intervals of (1) and (2). For the energy range defined by (4), the significance is only computed for the first four time intervals.

5.3. Star Formation Rate Selection

As magnetars are thought to originate from core collapse supernovae, and considering that MGFs can only be produced by young magnetars, it is expected that MGFs originate preferably in galaxies with a large star formation rate (SFR), similar to long GRBs. Approximately 64 % of the galaxies in the LV catalog have a measured value for the SFR, either originating from the H_α line emission or the far ultraviolet (FUV) continuum luminosity.

The galaxy with the smallest SFR that was proposed in previous work as host galaxy for MGFs is the Andromeda Galaxy with an H_α SFR of $0.5 M_\odot \text{ yr}^{-1}$ and FUV SFR of $1.0 M_\odot \text{ yr}^{-1}$. These two values were used as thresholds for the galaxies. All

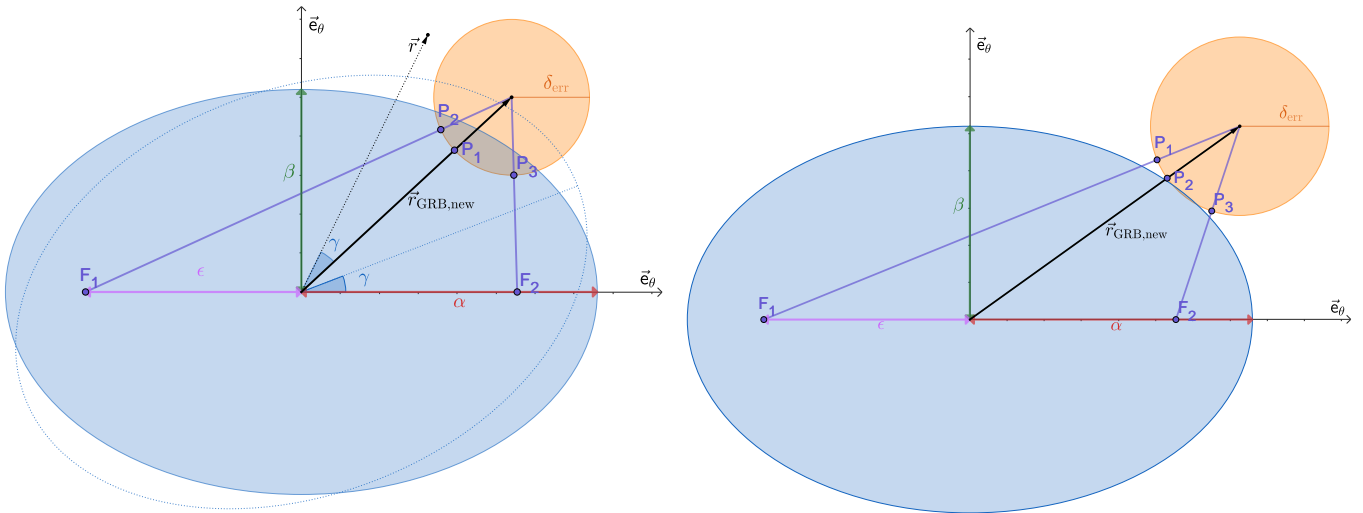


Fig. 4. Two-dimensional illustration of an elliptical galaxy (blue) and uncertainty circle of a GRB (orange). The shape of the elliptical galaxy is given by the angular minor axis α and major axis β . F_1 and F_2 denote the focus points of the ellipse. The galaxy's orientation in the e_ϕ and e_θ plane is given by the angle γ . To account for the orientation of the galaxy on the sky, given by γ , the vector \mathbf{r} , that is highlighted with a dotted line, is rotated by the same angle in the opposite direction, yielding $\mathbf{r}_{\text{GRB,new}}$. **Left:** Case in which the galaxy's ellipse and the GRB's error circle intersect, all three points P_1 , P_2 and P_3 lie within the galaxy's ellipse, and thus an association of the GRB with the galaxy is considered. **Right:** Exceptional case in which all three intersection points P_1 , P_2 , and P_3 lie outside the ellipse but the circle and ellipse have a small intersection area nonetheless. An association between the GRB and the galaxy is excluded.

coinciding galaxies with an SFR that is smaller than the given values by the Andromeda Galaxy are discarded, as they are assumed unlikely to host MGFs. If no value for the SFR is given in the LV galaxy catalog, or an upper limit that is larger than the threshold, the galaxy is not excluded as potential host association.

5.4. Duration Selection

MGFs are expected to be short pulses, and are mainly searched for in catalogs of sGRBs which are traditionally defined with a duration less than 2 s. As we sample the duration of the simulated sGRBs from the full, non-truncated best-fit distribution, the duration can also be larger than 2 s. To mimic the selection, another cut on the simulated GRBs can be performed by choosing only GRBs with smaller durations than 2 s.

5.5. Isotropic Energy Release Selection

Another selection can be applied after computing the isotropic energy, which is given by Eq. (11). When using the spatial selection, the GRB's host is associated to be the found LV galaxy for the selected GRBs. Thus, for the luminosity distance d_L of the GRB, the distance to the corresponding associated galaxy is used instead of the true distance, given by the sampled redshift. Assuming that there is a maximum on the magnetic field strength in a magnetar that can power an MGF, the measured maximum isotropic energy release, $E_{\text{iso,max}} = 5.3 \times 10^{46}$ erg of MGF051103 (Ofek et al. 2006), is used as a threshold for the selection of MGF candidates.

5.6. Fluence Selection

If a GRB has a localization error in the order of degrees, an association with a specific galaxy becomes unlikely. All previously proposed extragalactic MGFs were detected with multiple instruments in the Interplanetary Network (IPN). With the tri-

angulation method, the localization of the triggered events can be improved to yield error boxes in the arcmin or even arcsec range. The typical error for the measurements of γ -rays with GBM alone are in the order of degrees. The detection of GRBs in the X-rays with Swift/BAT can also yield localizations in the arcmin range but the instrument detects on average 2.5 times less sGRBs than Fermi/GBM, which is why we do not focus on Swift observations in this work. A detailed summary of the localization methods of all current and future γ -ray instruments, and their accuracy, is given in Greiner et al. (2022).

So, when simulating GBM sGRBs with a small or no localization error, this would be only feasible if an IPN localization exists. However, not for all sGRBs that are detected by GBM, a localization with the IPN is possible. The detection probability of all instruments in the IPN scales with the fluence of the source, which denotes the time-integrated measured flux in a specific energy interval. The IPN efficiency is equal or larger than 50 % for a fluence equal or larger than 10^{-6} erg cm^{-2} (Hurley et al. 2013). The efficiency was computed in Hurley et al. (2013) for two cases, in the first for the measurement of the γ -rays with any two spacecrafts of the IPN, and in the other for two widely spaced instruments. The precision of the localization with triangulation is proportional to the distance of the spacecrafts. We only consider the case of two widely separated spacecrafts as only in this case can the localization error be efficiently decreased. We make a final selection by using the fluence threshold of $>10^{-6}$ erg cm^{-2} to choose the sGRBs with a high potential for a localization with the IPN and a decreased localization error.

6. Model checking

We performed three tests to verify that the population synthesis produces results that are in agreement with observations of sGRBs. To do so, we simulate a full survey of GRBs corresponding to an observation time frame of 14 years (the active time of GBM) in a comoving volume of up to redshift $z = 5$.

In the first test (Sect. 6.1), our aim is to determine whether the number of simulated sGRBs which are selected by the simulated GBM trigger is in agreement with the number of detected GRBs during the observation time of 14 years with GBM. Afterwards (Sect. 6.2), we show the sGRB population parameter distributions to validate that the sampled parameters follow the chosen distributions. In the third test (Sect. 6.3), we aim to check whether the input spectral parameters for each GRB can be recovered when using the previously described analysis methodology.

6.1. Number of GRBs

Integrating the spatial distribution as in Equation (7) and using the parameter values of case (c) as in Ghirlanda et al. (2016) with $\rho_0 \Delta t_{\text{obs}} = 11.2 \text{ Gpc}^{-3}$ yields the volume integral of 1676.3. As the measurement of GRBs in a given time interval is equivalent to a counting experiment, the number of GRBs in a survey is drawn from a Poisson distribution with the expected value given by the volume integral result $\lambda = 1676.3$.

In the test universe, 1623 GRBs were simulated of which only 157 were selected by the implemented GBM trigger. In contrast, the median best-fit lognormal distribution of the GRBs' duration T_{90} suggests that there are around 724 sGRBs in the GBM sample. Thus, almost five times more GRBs were detected in the past 14 years than our simulations predict. The reason for the mismatch between the number of detected GRBs from the simulated sample in comparison to the observed GBM sample is most likely due to an underestimated normalization constant of the spatial distribution used in Ghirlanda et al. (2016). Previous predictions for the redshift distribution of sGRBs differ by a factor of 300 (comparing results of Dominik et al. (2013) and Ghirlanda et al. (2016)). Even the two different assumptions of the E_p - E_{iso} and E_p - L_{iso} correlation, and the independent probability distribution in Ghirlanda et al. (2016), yield values for the normalization constant that differ by a factor of four.

The reason for the underestimated value of the normalization constant in Ghirlanda et al. (2016) is most likely based on selection effects. Instead of using a forward-folding model as we are using, Ghirlanda et al. (2016) assume that their chosen sample of sGRBs is representative for the entire population of sGRBs.

Therefore, we increased the normalization constant in the following analysis to $\rho_0 \Delta t_{\text{obs}} = 57 \text{ Gpc}^{-3}$ so that the number of detected sGRBs is in a similar range as the measured number of sGRBs (724) in the lifetime of GBM.

6.2. Population Parameter Distributions

Using the increased normalization constant of the redshift distribution, the normalized histograms for all parameters characterizing a full universe of sGRBs are shown in Fig. 5. In this test universe, 8440 GRBs were simulated, and 805 were selected by the GBM trigger. This is in a similar range as the number of detected sGRBs with GBM. As visible in Fig. 5, the sampled parameters follow the chosen probability density functions. As expected, there is a bias towards the observation of sGRBs with a small distance, namely small redshift (see panels (a) and (g) in Fig. 5) which is due to the measured flux scaling by the luminosity distance squared which is dependent on redshift. The farther away an sGRB is, the dimmer it is and the more unlikely is its detection. We find another bias on the detection of bright sources with larger luminosity and flux (see Fig. 5 (b) and (g)), which agrees with expectations too. The brighter a source is, the

more likely its detection is. Furthermore, GRBs with a preferably longer duration are detected (see Fig. 5 (f)) which is due to GBM's trigger algorithm, and its limited time resolution.

6.3. Recovering Population Parameters from Simulated GBM Data

In addition, we tested whether the input latent parameters of the sGRBs can be recovered when analyzing the simulated GBM data as described in Section 4, and thus if our simulations are consistent. Not for all GRBs that trigger GBM can a spectrum be fit. The more source counts are measured above the background, the more likely it is that the fit converges. It was found that for approximately 75 % of the simulated GRBs that were identified by the GBM trigger algorithm as detected, a spectrum could be fit. For about 90 % of the sGRBs for which the fitting process failed, the Bayesian blocks technique could not determine a source time interval. For the other sGRBs, the fitting algorithm did not converge and thus failed.

We randomly choose a detected GRB from the test universe which is representative for the other simulated and detected sGRBs for which a spectrum was fitted successfully. The chosen simulated GRB is at redshift $z = 0.60$ and has a duration of 0.65 s. Its sampled flux is $8.12 \times 10^{-6} \text{ erg cm}^{-2} \text{ s}^{-1}$. The latent spectral parameters of the chosen GRB's spectrum are the peak energy in the burst frame $E_p = 788 \text{ keV}$ and the power law index $\alpha = -0.82$. In the observer frame, the peak energy is shifted to lower energies $E_{p,\text{obs}} = E_p / (1 + z)$, and is thus at $E_{p,\text{obs}} = 486.25 \text{ keV}$.

Using `gbmgeometry`, the closest BGO and the three closest NaI detectors can be determined which have the smallest separation angle between their pointing and the direction of the GRB. For the test GRB, the closest BGO detector is b_0 , and the closest NaI detectors are in descending order n_1 , n_0 and n_3 .

With the Bayesian blocks technique, the source interval was found to have a duration of 0.65 s, which is the same as the latent duration of the sGRB. A CPL spectrum as parameterized in Equation (2) is fit with 3ML to the counts that were measured in the set source interval. The corner plot of the CPL fit for the chosen GRB is shown in Fig. 6. The modes of the marginal posterior distributions of the fit match the latent parameters.

7. Simulations and Results

First, we studied how the number of spatial coincidences changes as a function of the angular error radius of the sGRB localization. Then, we assume that the localization of the sGRBs has no uncertainties, corresponding to the existence of an IPN localization with errors in the order of arcmin or even arcsec. We simulate 1000 surveys of sGRBs with a constant temporal profile. For the redshift and luminosity distribution, we use the parameters of Ghirlanda et al. (2016), as summarized in Table 2, except that we use the increased normalization constant $\rho_0 \Delta t_{\text{obs}} = 57 \text{ Gpc}^{-3}$ for the redshift distribution, as described in Sec. 6.1. For the GRBs coinciding with a LV galaxy, we simulate GBM data, run the GBM trigger algorithm, and search for MGF candidates, based on the selection criteria that we described in Sec. 5. The results of these simulations are summarized in the following.

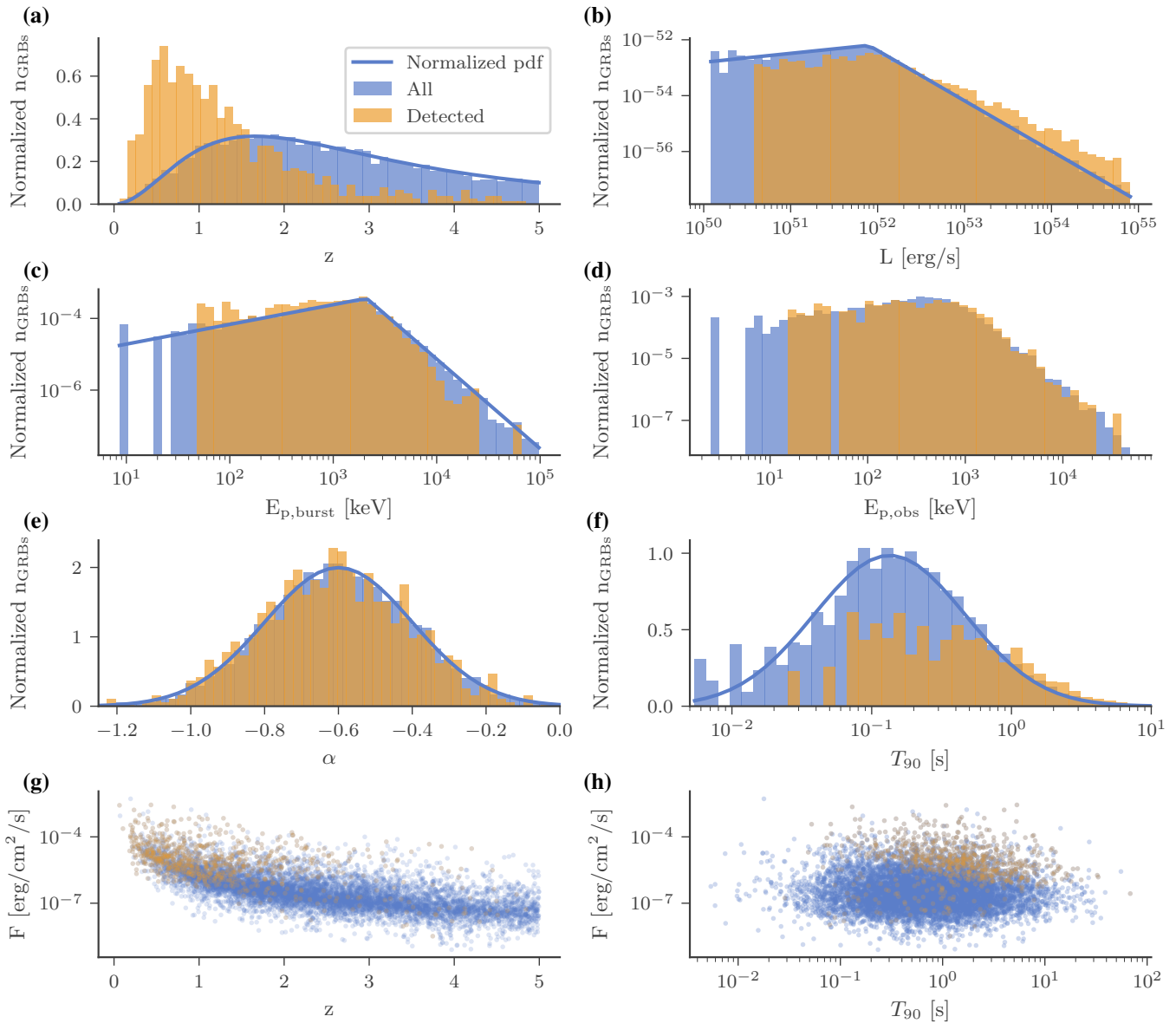


Fig. 5. Normalized density histograms of the simulated redshift z (a), luminosity L (b), peak energy $E_{p,burst}$ in the burst frame (c) and $E_{p,obs}$ in the observer frame (d), the power-law index α (e) and the duration T_{90} (f). Solid lines display the chosen probability density functions as described in Section 2, using the parameters corresponding to case (c) of Ghirlanda et al. (2016), and an increased value for the redshift normalization constant of $\rho_0 \Delta t_{obs} = 57 \text{ Gpc}^{-3}$. **Blue:** All simulated GRBs. **Orange:** From GBM trigger selected GRBs. The histograms are normalized by dividing each bin by the bin width in such a way that their integral yields unity. The lower panels (g) and (h) show the scatter of the simulated flux as a function of the redshift and duration on the left and right respectively.

7.1. Spatial Selection

To study how the number of spatial coincidences changes as a function of the error on the sGRB localization, we simulate 50 surveys of sGRBs assuming different uncertainty radii around the simulated true location of the sGRBs. We compute the number of spatial coincidences in each of the surveys. In the left panel of Fig. 7, one simulation of a population of sGRBs with an error circle of radius 1° is shown. In the example, 8440 sGRBs were simulated, of which 337 could be associated with at least one galaxy of the LV catalog.

The number of spatial coincidences in the simulated surveys as a function of the uncertainty of the GRB localization is shown in Figure 8. Up to an error radius of about $0.03^\circ = 1.8 \text{ arcmin}$, the uncertainty of the GRB's localization does not affect the

number of coincidences significantly and is thus independent of the localization error. As the positions of the GRBs are sampled in such a way that they are isotropically distributed at the sky, the number of spatial coincidences is expected to be only dependent on the angular fraction of the sky that is covered by the nearby galaxies and the number of GRBs in the survey. Thus, the expected number of coincidences is given by

$$n_{\text{coinc, exp}} = N \frac{\sum_{i=1}^{N_{LV}} \pi a_i b_i}{4\pi}, \quad (15)$$

where N is the expected number of sGRBs in a survey which is given by the volume integral in Eq. (7). As visible in Fig. 8, the number of spatial coincidences scatters around the expected number $n_{\text{coinc, exp}}$.

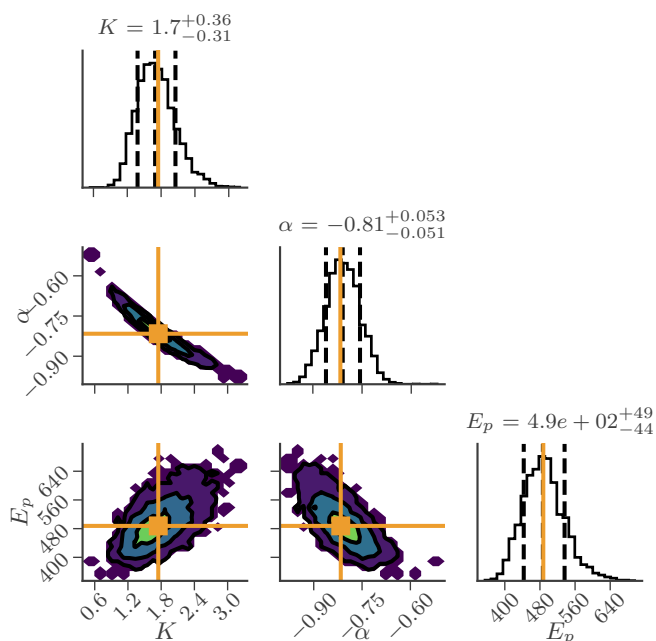


Fig. 6. Corner plot of the CPL fit of the test GRB. The CPL is parameterized as in Equation (2) with $E_{\text{piv}} = 1$ keV. The peak energy E_p has units of keV, the power law index is unit-less and the normalization K has units of $\text{cm}^{-2} \text{s}^{-1} \text{keV}^{-1}$. The true chosen parameters are highlighted in orange.

For larger error radii, the number of spatial coincidences rises as a power of the circular error radius. By increasing the error radius by one order of magnitude from 0.1° to 1° , the number of coincidences rises approximately by a factor of 40, so more than an order of magnitude.

If the localization error is large, an association of a GRB with a specific galaxy becomes unlikely as there are too many galaxies in the field of view. The localization region of all previously proposed MGF candidates was in the order of arcmin as they all had an IPN localization. This corresponds to the region in which the number of spatial coincidences is independent of the GRB's localization error. In the following, we simulate 1000 surveys in which we set the error radius to zero, thus assuming that there is an IPN localization for all sGRBs. We select only the sGRBs that are spatially coinciding with one of the LV galaxies.

7.2. SFR Selection

We apply a selection on the coinciding galaxies based on their SFR. All coinciding galaxies with an SFR that is smaller than the SFR by the Andromeda Galaxy are discarded, as they are assumed unlikely to host MGFs. If no value for the SFR is given in the LV galaxy catalog, or an upper limit that is larger than the threshold, the galaxy is not excluded as potential host association.

Of all 1244 galaxies in the LV catalog, 162 different galaxies were at least once aligned with one of the sGRBs in the 1000 simulated surveys. Only 44 of the 162 galaxies (about 27 %) fulfill the SFR selection criterion, and can thus be considered as potential host galaxies for MGFs.

In Fig.9, a histogram of the 20 galaxies that most often align with the simulated sGRBs are shown. The number of spatial coincidences is summed over all simulated surveys. The galaxies fulfilling the SFR criterion are highlighted by filled bars. While

in the simulations, there was no chance coincidence of sGRBs with the galaxies M82 and M83, the other two galaxies (M31, NGC0253) that were proposed as hosts for the observed MGFs 070201 and 200415A belong to the 12 most often coinciding galaxies. Note here that in the literature, the galaxy associated with 200415A is called Sculptor but is named NGC0253 in the LV catalog. The galaxy named Sculptor in the LV catalog is a different galaxy which is excluded as host for MGFs because of its small SFR.

How often an sGRB coincides with a galaxy is proportional to its angular size. The number of spatial coincidences as a function of the galaxies' angular area and distance is shown in the right panel of Figure 10. By far the most spatial coincidences are in association with the Sagittarius Dwarf Galaxy (SagdSph). In comparison to the second most often associated galaxy, Antlia 2, the number of associations with the Sagittarius Galaxy is larger by an order of magnitude, and thus dominates the result. The Sagittarius Galaxy is also by far the largest galaxy on the sky after excluding the Small and Large Magellanic Cloud from the LV catalog. As there is no constraint on the SFR given for the Sagittarius Galaxy, we do not remove the galaxy from the LV sample.

7.3. GBM Trigger Selection

In Fig.11, it is shown in how many surveys we find a specific number of spatial coincidences of sGRBs and LV galaxies. In 99.9 % of all simulated sGRB surveys, at least one of the GRBs coincides with one of the galaxies in the LV catalog. Of the 5469 sGRBs in all 1000 simulated surveys that coincide with a LV galaxy, 524 are detected by the GBM trigger algorithm. There are 411 surveys in which at least one detected GRB coincides with a nearby galaxy. Thus, when only considering the spatial and GBM trigger selection, there is a chance of about 41 % that in the observing duration of 14 years, there is at least one sGRB detected that can be falsely associated with a nearby galaxy.

The number of coincidences is directly proportional to the observing time as the number of GRBs in the universe is given by the integrated redshift distribution, which is proportional to the observation time (see Equation (7)). Thus, it can be computed after which observation time the probability is larger than 5 % to observe an MGF. After a detection time of approximately 1.7 years, GBM is triggered by an sGRB which is aligning by chance with a nearby galaxy with a probability of 5%. Of the 45 different galaxies that are found to be coinciding with detected sGRBs in all simulated surveys, 17 fulfill the SFR condition. The result is strongly dominated by the Sagittarius Galaxy.

When combining the spatial, GBM trigger, and SFR selection, we find coincidences in 298 surveys. Therefore, after 2.3 years, GBM observes with a 5% chance an sGRB that is coinciding with a nearby galaxy which has an SFR that is larger than the one from the Andromeda Galaxy. The result is strongly dominated by the Sagittarius Galaxy. Without the Sagittarius galaxy, GBM sees an sGRB with the described properties after 6.8 years with a 5% probability, and the detection probability after 14 years is 10.3 %.

7.4. Duration Selection

The distribution of the durations of sGRBs triggering GBM and coinciding with one of the LV galaxies is shown in Fig.12. The duration was determined by using the Bayesian block method. For about 74 % (386 sGRBs) of the detected sGRBs, the

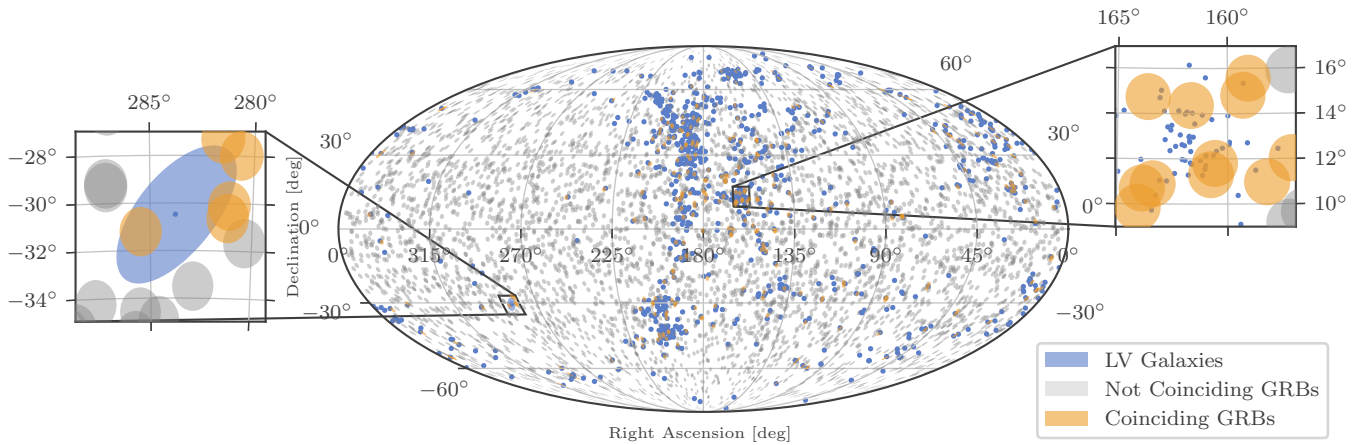


Fig. 7. Visualization of the locations of sGRBs on the sky in a simulated survey, in which an angular error radius of 1° for the localization of all sGRB is assumed. The coordinates are given in the International Celestial Reference System (ICRS). sGRBs coinciding with the position of a Local Volume Galaxy are highlighted in orange.

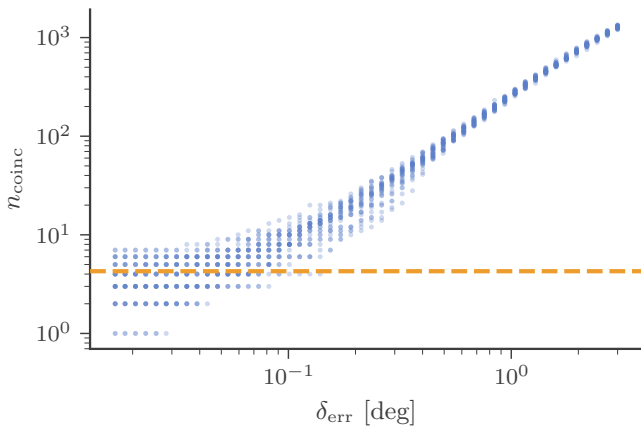


Fig. 8. Number of coincidences of the GRB's location with a galaxy in simulated surveys as function of the GRB's error circle radius δ_{err} . The scatter originates from the results of 50 surveys of sGRBs that were simulated for each chosen error circle. The orange line corresponds to the expected number of spatial coincidences at small error radii (see Eq. (15))

Bayesian block method was able to determine at least three time intervals, thus identifying a source interval in between the background intervals. The other 26 % of the sGRBs were discarded from the following analysis. As there is a bias towards measuring sGRBs with longer durations (see Fig.5), there is a non-negligible number of 148 sGRBs with a duration larger than 2 s.

After excluding the sGRBs with $T_{90} > 2$ s, we still find at least one MGF candidate in 226 surveys (22.6 % of all simulated surveys). When excluding the coincidences with the dominating Sagittarius Galaxy, in 85 surveys, there is at least one sGRB left that is selected by the spatial, GBM trigger, and duration selection criteria. A MGF candidate is found by chance after 3.1 years with 5 % probability when only considering events that trigger GBM and have a duration smaller than 2 s.

When combining the duration selection with the SFR selection, the detection probability of an MGF candidate is 20.5 %, without the Sagittarius Galaxy 6.2 %. Hence, GBM is triggered

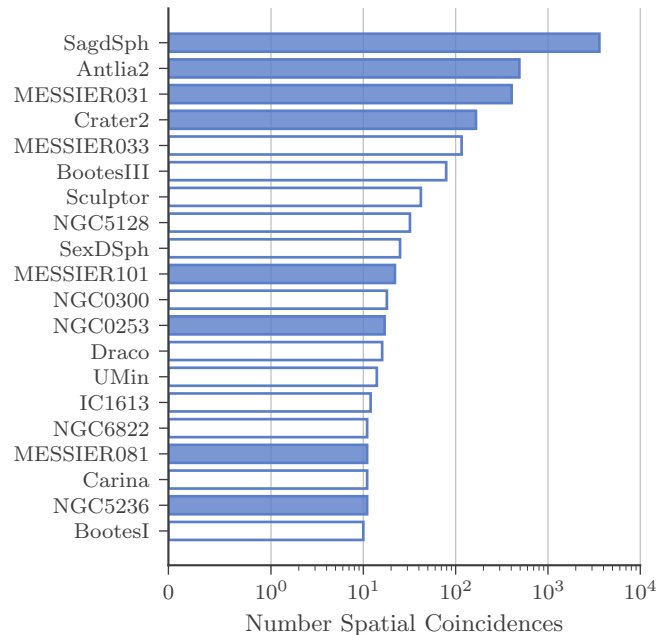


Fig. 9. Number of spatial coincidences summed over all surveys of GRBs for the 20 most often coinciding galaxies in all 1000 simulated surveys. Galaxies fulfilling the SFR selection criteria are highlighted by filled bars. Excluded galaxies are illustrated by unfilled bars.

with a non-negligible probability of 5 % after approximately 3.4 years by an sGRB that can be wrongly associated as MGF, and when neglecting the Sagittarius Galaxy as host, after 11.3 years.

7.5. Isotropic Energy Release Selection

One of the main arguments for the candidacy of proposed extragalactic MGFs was that the determined peak energy and isotropic energy release of the candidates was not consistent with the measured population of sGRBs. However, this relies on the presumption that the distance to the events is that of the assumed nearby host galaxy. This results in the peak and isotropic energy being scaled to this nearby distance rather than that of a possibly more distant origin.

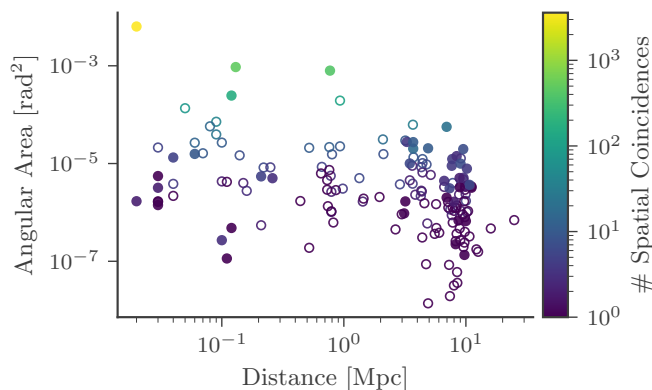


Fig. 10. Number of spatial coincidences summed over all surveys as a function of the angular area and distance of the galaxies. Galaxies fulfilling the SFR selection criteria are highlighted by filled circles. Excluded galaxies are illustrated by unfilled circles.

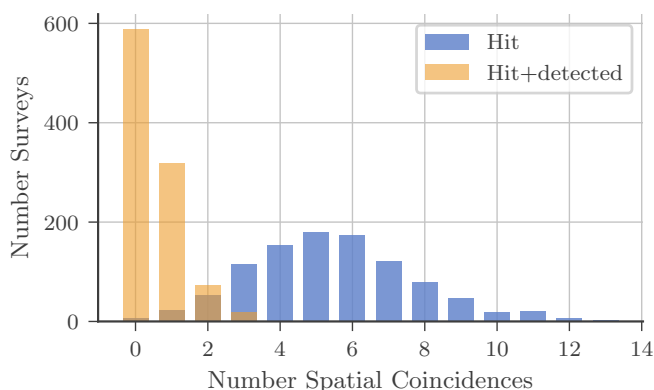


Fig. 11. **Blue:** Number of surveys in which a specific number of sGRBs coincided with the location of a nearby galaxy. **Orange:** sGRBs that were selected by the GBM trigger algorithm in addition to coinciding with a galaxy.

For all 386 simulated sGRBs which coincide with the location of a nearby galaxy, which are selected by the GBM trigger algorithm, and for which the spectral fit succeeded, we computed the isotropic energy release and peak energy. First, we assume that the host of the GRB is at the distance given by the coinciding nearby galaxy. Second, we assume that the latent redshift of all GRBs could be correctly determined and scale the isotropic energy and peak energy to the luminosity distance given by the redshift. The E_p - E_{iso} scatter plot for both cases is shown in Figure 13. The results when using the latent redshift are highlighted in orange, and for the assumed distance to the LV galaxies in blue. In addition to the results of the simulated data, the results for E_p and E_{iso} of all identified sGRBs by Konus Wind (Tsvetkova et al. 2017), and GBM (Poolakkil et al. 2021) are depicted. If the redshift of the sGRBs is able to be correctly determined, E_p and E_{iso} are in agreement with the measured sGRB population from Konus Wind and GBM, as there are no far outliers. In contrast, if the distance to the coinciding nearby galaxy is used, the points indeed look like a separate population that is not in agreement with the sGRB population. Nevertheless, the difference is only due to the extremely underestimated value for the distance of the sGRBs, and is thus an artifact of the wrong host association.

Using the maximum value for the isotropic energy of 5.3×10^{46} erg (the highest ever derived for an MGF), 381 sGRBs

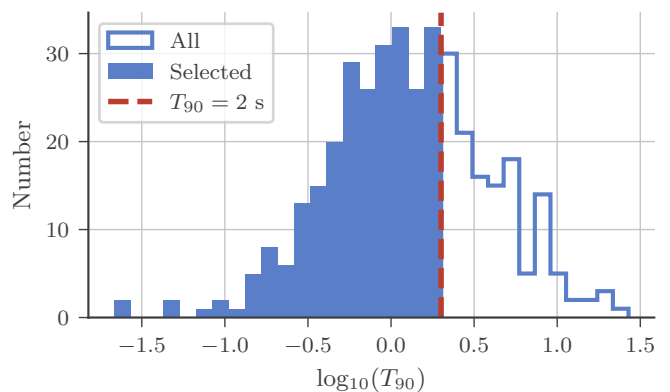


Fig. 12. Histogram of the logarithmic durations of all sGRBs triggering GBM and coinciding with a LV galaxy. sGRBs with $T_{90} < 2$ s are selected (filled histogram), the others are discarded (unfilled histogram). The threshold is highlighted by a red dashed vertical line.

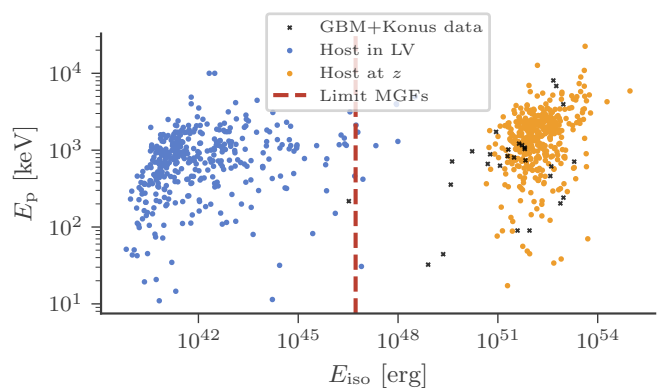


Fig. 13. Scatter plot of the simulated peak energy E_p and isotropic energy release E_{iso} assuming a distance given by the coinciding LV galaxy (**blue**), and by the simulated redshift (**orange**). The black crosses correspond to the determined values for E_p and E_{iso} of sGRBs that were observed by GBM (Poolakkil et al. 2021) and Konus Wind (Tsvetkova et al. 2017), respectively.

are compatible with MGFs when setting the distance to the ones of the coinciding galaxies. If in contrast the redshift of the sGRBs is known, all sGRBs have an isotropic energy that is larger than the limit given by the magnetic field strength, which is not compatible with the interpretation as MGFs.

When using the spatial, GBM trigger, and isotropic energy selections for identifying MGFs, we find in 30.4 % of all simulated surveys, one or more accidental MGF candidates. When excluding the Sagittarius Galaxy from the analysis, we find accidental MGF candidates in 11 % of the surveys. After 2.3 years of observing with GBM, an accidental MGF candidate can be identified with a probability of 5 %, and when excluding the Sagittarius galaxy after 6.4 years.

Combining the selection on E_{iso} with the duration T_{90} and SFR selection yields MGF candidates in 20.3 % of the surveys if the Sagittarius Galaxy is included the computations, and 6.0 % if the galaxy is excluded. A detection of an sGRB fulfilling the spatial, E_{iso} , T_{90} and SFR condition is detected with a 5 % probability after 3.4 years of observation time, and when excluding the Sagittarius galaxy after 11.7 years.

7.6. Fluence Selection

As a final selection, we use a threshold for the fluence of 10^{-6} erg cm $^{-2}$ to incorporate the IPN efficiency at higher fluences of the source. When only considering the spatial and fluence selection, GBM has a 5 % detection probability after 2.6 years, and when excluding the Sagittarius Galaxy after 7.1 years.

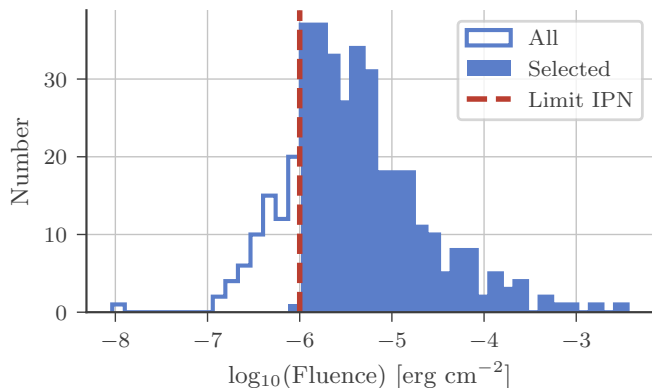


Fig. 14. Histogram of the fluence of the simulated sGRBs that coincide with a nearby galaxy, and are selected by the GBM trigger algorithm.

Finally, combining all proposed selections, namely the spatial, SFR, T_{90} , E_{iso} , and fluence selection, yields in 15.7 % of the simulated surveys coincidences in 9 different host galaxies. When excluding the Sagittarius Dwarf galaxy as host, there is only a 4.3 % chance for chance coincidences. After an observation time of 16.3 years, there is a 5 % chance for coincidences, which is soon reached.

In Table 3, a summary of the results of all combinations of selections is given.

8. Conclusions

In summary, after an exhaustive list of selections are applied to our simulations, namely the spatial, GBM trigger, GBM duration T_{90} , isotropic energy release E_{iso} , and fluence selection, the probability of detecting an sGRB which could be potentially misidentified as an extragalactic MGF is 15.7 %. When excluding the dominating Sagittarius Galaxy, the probability of detecting an sGRB that fulfills all six criteria reaches the 5 % level after an observation period of about 16 years, which is not far in the future. While the analysis cannot prove that a specific one of the previously proposed MGFs are sGRBs, it attempts to integrate over the probability of a misidentification by simulating an alternative hypothesis. Thus, any significance of true association must incorporate the possibility that the event is actually an sGRB.

The number of coincidences grows as a power function of the error circle size of the sGRBs localization for error circles larger than approximately 1.8 arcmin. While improving the localization decreases the number of galaxies in the field of view, we showed that this is not enough to distinguish MGFs from sGRBs.

Hence, for the unambiguous identification of extragalactic MGFs in the future, it will be necessary to find other criteria. Such a criterion is for example the pulsating tail in the measured light curve, as clearly detected for the galactic MGFs. The oscillations in the tail are not characteristic of sGRBs, and could thus distinguish sGRBs from MGFs. However, when MGFs originate from larger distances, it becomes less likely that the pulsating tail is detectable.

A direct proof of an association of an MGF with a LV galaxy would be given by measuring the distance to the source, which can be derived from measuring the redshift. Thus, fast follow up observations in other wavelengths, especially in the optical, and determining the redshift is important to identify the gamma-rays' source. It is indeed true that many of the properties assigned to current candidate MGFs rely entirely on the host galaxy's distance which can lead to circular reasoning.

We conclude that an association of γ -ray sources with LV galaxies does not necessitate the progenitor to be an MGF as there is a non-negligible probability of the progenitor being an sGRB at larger distance behind the LV galaxy along the line of sight. sGRBs can reproduce the same typical characteristics of the measured γ -ray sources that were associated with magnetars. Indeed, similar considerations for other spatial and/or temporal coincidence should be made in order to minimize the chances of false associations. For example, nearly all distances to sGRBs have been determined by assuming that a spatially projected nearby galaxy is the host and thus this galaxy's redshift is used for the sGRB. Our study could be adapted to compute how likely this host association is made by chance coincidence when, for example, the sGRB's true host is a more distant and undetected galaxy, or alternatively a much closer and low-mass, low surface-brightness undetected galaxy.

All code required to reproduce this work is distributed freely ⁸.

Acknowledgements. We thank Bjoern Biltzinger and Aaron Tohuvavohu for discussions. The final writing of this paper was funded by the Federal Ministry of Education and Research (BMBF) and the Baden-Württemberg Ministry of Science as part of the Excellence Strategy of the German Federal and State Governments. JMB acknowledges support from the Alexander von Humboldt Foundation and the DFG-funded Collaborative Research Center 1258.

References

- Abbott, B. P., Abbott, R., Abbott, T. D., et al. 2017, *Phys. Rev. Lett.*, 119, 161101
- Barat, C., Hayles, R. I., Hurley, K., et al. 1983, *A&A*, 126, 400
- Buchner, J., Georgakakis, A., Nandra, K., et al. 2014, *A&A*, 564, A125
- Burgess, J. & Capel, F. 2021, *The Journal of Open Source Software*, 6, 3257
- Burgess, J. M., Cameron, E., Svinkin, D., & Greiner, J. 2021, *A&A*, 654, A26
- Burgess, J. M., Greiner, J., Bégué, D., & Berlato, F. 2019, *MNRAS*, 490, 927
- Burns, E., Svinkin, D., Hurley, K., et al. 2021, *ApJ*, 907, L28
- Carpenter, B., Gelman, A., Hoffman, M. D., et al. 2017, *Journal of Statistical Software*, 76, 1–32
- Cenko, S. B., Ambrosi, E., Barthelmy, S. D., et al. 2022, *GRB Coordinates Network*, 32191, 1
- Cole, S., Norberg, P., Baugh, C. M., et al. 2001, *MNRAS*, 326, 255
- D'Avanzo, P., Salvaterra, R., Bernardini, M. G., et al. 2014, *MNRAS*, 442, 2342
- Day, A., Schlegel, D. J., Lang, D., et al. 2019, *AJ*, 157, 168
- Dominik, M., Belczynski, K., Fryer, C., et al. 2013, *ApJ*, 779, 72
- Duncan, R. C. & Thompson, C. 1992, *ApJ*, 392, L9
- Evans, W. D., Klebesadel, R. W., Laros, J. G., et al. 1980, *ApJ*, 237, L7
- Fermi-LAT and GBM Collaboration. 2022, *Gamma Ray Burst Observations*, <https://fermi.gsfc.nasa.gov/ssc/observations/types/grbs/>
- Feroz, F., Hobson, M. P., & Bridges, M. 2009, *MNRAS*, 398, 1601
- Frederiks, D. D., Hurley, K., Svinkin, D. S., et al. 2013, *ApJ*, 779, 151
- Ghirlanda, G., Salafia, O. S., Pescalli, A., et al. 2016, *A&A*, 594, A84
- Greiner, J., Burgess, J. M., Savchenko, V., & Yu, H. F. 2016, *ApJ*, 827, L38
- Greiner, J., Hugentobler, U., Burgess, J. M., et al. 2022, *A&A*, 664, A131
- Guetta, D. & Piran, T. 2005, *A&A*, 435, 421
- Guetta, D. & Piran, T. 2006, *A&A*, 453, 823
- Hurley, K., Boggs, S. E., Smith, D. M., et al. 2005, *Nature*, 434, 1098
- Hurley, K., Cline, T., Mazets, E., et al. 1999, *Nature*, 397, 41
- Hurley, K., Pal'shin, V. D., Aptekar, R. L., et al. 2013, *ApJS*, 207, 39
- Israel, G. L., Belloni, T., Stella, L., et al. 2005, *ApJ*, 628, L53
- Kaisina, E. I., Makarov, D. I., Karachentsev, I. D., & Kaisin, S. S. 2012, *Astrophysical Bulletin*, 67, 115
- Karachentsev, I. D., Karachentseva, V. E., Huchtmeier, W. K., & Makarov, D. I. 2004, *AJ*, 127, 2031

⁸ https://github.com/grburgess/grb_shader

Table 3. Summary of all results when applying the GBM Trigger, SFR, T_{90} , E_{iso} , and fluence selections. The second and third column summarize the probability for misidentifying an sGRB as magnetar in an observation period of 14 years given the chosen selection criteria. The last two columns show the observation time with GBM that yields a 5 % detection probability of sGRBs with the chosen characteristics.

Selection	Misidentification probability (all) [%]	Misidentification probability (without SagdSph) [%]	Observation time until 5% probability (all) [yr]	Observation time until 5% probability (without SagdSph) [yr]
GBM	41.1	15.3	1.7	4.6
GBM, SFR	29.8	10.3	2.3	6.8
GBM, T_{90}	22.6	8.5	3.1	8.2
GBM, SFR, T_{90}	20.5	6.2	3.4	11.3
GBM, E_{iso}	30.4	11.0	2.3	6.4
GBM, SFR, E_{iso}	28.0	7.7	2.5	9.1
GBM, SFR, E_{iso} , T_{90}	20.3	6.0	3.4	11.7
GBM, Fluence	26.6	9.8	2.6	7.1
GBM, Fluence, T_{90}	17.7	6.5	4.0	10.8
GBM, Fluence, E_{iso}	25.8	9.0	2.7	7.8
GBM, Fluence, SFR	23.8	6.3	2.9	11.1
GBM, Fluence, T_{90} , E_{iso}	17.2	6.0	4.1	11.7
GBM, Fluence, T_{90} , SFR	15.9	4.5	4.4	15.6
GBM, Fluence, E_{iso} , SFR	23.5	6.0	3.0	11.7
GBM, Fluence, T_{90} , E_{iso} , SFR	15.7	4.3	4.5	16.3

- Levan, A. J., Malesani, D. B., Gompertz, B. P., & a larger Collaboration. 2022, GRB Coordinates Network, 32262, 1
- Li, T. P. & Ma, Y. Q. 1983, ApJ, 272, 317
- Mandhai, S., Tanvir, N., Lamb, G., Levan, A., & Tsang, D. 2018, Galaxies, 6, 130
- Mazets, E. P., Aptekar, R. L., Cline, T. L., et al. 2008, ApJ, 680, 545
- Mazets, E. P., Cline, T. L., Aptekar, R. L., et al. 1999, Astronomy Letters, 25, 635
- Mazets, E. P., Golenetskii, S. V., Ilinskii, V. N., et al. 1981, Ap&SS, 80, 3
- Mazets, E. P., Golenetskii, S. V., Ilinskii, V. N., Aptekar, R. L., & Guryan, I. A. 1979, Nature, 282, 587
- Meegan, C., Lichti, G., Bhat, P. N., et al. 2009, ApJ, 702, 791
- Mereghetti, S., Götz, D., von Kienlin, A., et al. 2005, ApJ, 624, L105
- Metzger, M. R., Djorgovski, S. G., Kulkarni, S. R., et al. 1997, Nature, 387, 878
- Nakar, E., Gal-Yam, A., & Fox, D. B. 2006, ApJ, 650, 281
- Ofek, E. O., Kulkarni, S. R., Nakar, E., et al. 2006, ApJ, 652, 507
- Ofek, E. O., Muno, M., Quimby, R., et al. 2008, ApJ, 681, 1464
- Paciesas, W. S., Meegan, C. A., von Kienlin, A., et al. 2012, ApJS, 199, 18
- Palmer, D. M., Barthelmy, S., Gehrels, N., et al. 2005, Nature, 434, 1107
- Poolakkil, S., Preece, R., Fletcher, C., et al. 2021, ApJ, 913, 60
- Pumpe, D., Gabler, M., Steininger, T., & EnBlin, T. A. 2018, A&A, 610, A61
- Rastinejad, J., Levan, A. J., Malesani, D. B., et al. 2022, GRB Coordinates Network, 32208, 1
- Roberts, O. J., Veres, P., Baring, M. G., et al. 2021, Nature, 589, 207
- Scargle, J. D., Norris, J. P., Jackson, B., & Chiang, J. 2013, ApJ, 764, 167
- Schneider, B., Malesani, D. B., Fynbo, J. P. U., et al. 2022, GRB Coordinates Network, 32595, 1
- Strohmayer, T. E. & Watts, A. L. 2005, ApJ, 632, L111
- Svinkin, D., Frederiks, D., Hurley, K., et al. 2021, Nature, 589, 211
- Svinkin, D. S., Hurley, K., Aptekar, R. L., Golenetskii, S. V., & Frederiks, D. D. 2015, MNRAS, 447, 1028
- Tanvir, N. R., Chapman, R., Levan, A. J., & Priddey, R. S. 2005, Nature, 438, 991
- Thompson, C. & Duncan, R. C. 1993, ApJ, 408, 194
- Tikhomirova, Y. Y., Pozanenko, A. S., & Hurley, K. S. 2010, Astronomy Letters, 36, 231
- Tsvetkova, A., Frederiks, D., Golenetskii, S., et al. 2017, ApJ, 850, 161
- Vianello, G., Lauer, R. J., Younk, P., et al. 2015, arXiv e-prints, arXiv:1507.08343
- Virgili, F. J., Zhang, B., O'Brien, P., & Troja, E. 2011, ApJ, 727, 109
- von Kienlin, A., Meegan, C. A., Paciasas, W. S., et al. 2020, ApJ, 893, 46
- Wanderman, D. & Piran, T. 2015, MNRAS, 448, 3026
- Watts, A. L. & Strohmayer, T. E. 2006, ApJ, 637, L117
- Yu, H.-F., Preece, R. D., Greiner, J., et al. 2016, A&A, 588, A135